*J Mater Sci* (2023) 58:10023–10042

Computation & theory

# Unveiling the properties of transition-metal dichalcogenides: a comprehensive study of $WTe_2$, $WSe_2$, $ZrTe_2$, and $NiTe_2$ in bulk and monolayer forms

Yasaman Fazeli[1], Zeynab Etesami[1], Zahra Nourbakhsh[1,*], and Daryoosh Vashaee[2,3,*]

[1] Faculty of Physics, University of Isfahan, Isfahan 81746-73441, Iran
[2] Department of Electrical and Computer Engineering, North Carolina State University, Raleigh, NC 27606, USA
[3] Department of Materials Science and Engineering, North Carolina State University, Raleigh, NC 27606, USA

**Received:** 27 January 2023
**Accepted:** 26 April 2023
**Published online:** 1 June 2023



## ABSTRACT

This study conducts a thorough examination of the properties of four transition-metal dichalcogenides (TMDCs): $WTe_2$, $WSe_2$, $ZrTe_2$, and $NiTe_2$, using first-principles density functional theory calculations. The results reveal that $WSe_2$ and $WTe_2$ exhibit semiconducting behavior in both bulk and monolayer forms, while $ZrTe_2$ and $NiTe_2$ exhibit metallic behavior in their bulk forms. However, a deviation from metallic behavior is observed in the monolayer form of $NiTe_2$. The study also delves into the optical characteristics of both bulk and monolayer forms, including dielectric function, reflectivity, absorption coefficient, refraction coefficient, and electron energy loss function. These findings provide a comprehensive understanding of the properties of these TMDCs, which can be utilized in the design of advanced optoelectronic devices. Moreover, the observed decrease in absorption coefficient in the monolayer forms of these TMDCs can be leveraged for transparent conductor technology. Overall, this study presents a detailed analysis of the properties of TMDCs, highlighting their potential for technological exploitation in a wide range of optoelectronic applications.

## Introduction

Transition-metal chalcogenides (TMDs) are a class of materials composed of transition metals and chalcogens (elements of group VIA) and have a wide range of essential applications [1–7]. TMDs are employed in electrochemical energy storage devices such as batteries and fuel cells and exhibit high thermoelectric performance in materials like bismuth telluride, lead telluride, and manganese telluride [8–18]. Their applications extend to thermal switches, sensors, and topological lasers [19–21] and as catalysts in chemical reactions, including hydrogenation and hydrodesulfurization [22–26]. They are also utilized in producing

Handling Editor: Kevin Jones.

Address correspondence to E-mail: z.nourbakhsh@sci.ui.ac.ir; dvashae@ncsu.edu

https://doi.org/10.1007/s10853-023-08545-w

thin-film transistors and other electronic devices. Some TMDs, such as niobium selenide and niobium sulfide, act as superconductors at low temperatures, making them suitable for various applications, including electrical power transmission and magnetic resonance imaging [27–29]. Recently, TMDs in IVB, VB, and VIB groups have gained significant attention due to their broad physical properties [21, 30, 31].

TMDs with the formula $MX_2$ consist of metal atoms M (e.g., Zr, W, Ni) and a chalcogen X (e.g., S, Se, Te). The metal atom M is sandwiched between the two anion surfaces of the X atom, forming a strong covalent metal anion bond between the metal atom M and the chalcogen atom X [32]. Owing to the d-orbitals involved in their electronic structure, TMDs have attracted heightened interest due to their remarkable range of electronic, optical, mechanical, and thermal properties [33–36]. These properties have led to advances in practical devices, such as field-effect transistors [37–42], photodetectors [43, 44], chemical [45] and biosensors [46, 47], and nanoelectromechanical systems (NEMS) [48–50]. Moreover, TMDs can exhibit metallic and semiconducting behavior, depending on their electronic properties, and can also be applied as dry lubricants due to their layered structures [51–53].

Recently, the scientific community has widely explored a vast number of 2D and layered materials, leading to numerous applications in nanoelectronics [54, 55], energy storage [56, 57], detection [58], gas separation [59], and solar energy conversion [60]. TMD semiconducting single crystals and transparent thin films have been used to fabricate high-efficiency solar cells, rechargeable batteries, and high-temperature solid lubricants [61]. Monolayer TMDs are uniquely suited for optoelectronic applications [62], field-effect transistors [37, 63, 64], and photovoltaic cells [65] due to their large direct bandgap. Additionally, monolayer TMDs have two degenerate valleys at the corners of the first Brillouin zone for both conduction and valence bands, crucial for optically controlling charge carriers in these valleys [66]. These properties enable the integration of new classes of spintronic and valleytronic devices [67, 68]. Detailed information about the optical and electronic properties of monolayer TMDs is highly desired for various applications and can be obtained by measuring or calculating the refractive index and extinction coefficient spectra of monolayer TMDs versus the frequency range.

Layered transition-metal dichalcogenides (TMDs), represented by the formula $MX_2$ (M=Zr, W, Ni, Mo, etc., X=Te, Se, S, etc.), have garnered significant attention from researchers in the field of 2D materials due to their remarkable properties [69–73]. Among these materials, $ZrTe_2$, $WTe_2$, $WSe_2$, and $NiTe_2$ stand out as fascinating members of the TMDs family. Each $MX_2$ layer is held together by strong covalent bonds, while interlayer bonds are maintained by weak van der Waals forces [74, 75]. This unique bonding structure results in various intriguing physical properties, rich intercalation chemistry, and numerous potential applications [76, 77]. TMDs typically crystallize with hexagonal symmetry and space groups (SG) P-3m1 and P63/mmc, which enable the intercalation of other atomic species and complexes in the region between adjacent chalcogen planes (van der Waals gap) [78–83]. Researchers have investigated other applications of TMDs, such as photocatalysis, optoelectronics, and photovoltaics [84–88]. However, many aspects of these materials remain unknown, limiting their potential applications.

$ZrTe_2$ and $NiTe_2$ crystallize in a trigonal structure (CdI2-type, SG P-3m1, number 164). A first-principles study has investigated the structural stabilities and electronic properties of $ZrX_2$ (X=S, Se, or Te) thin films of various thicknesses [89]. Angle-resolved photoemission spectroscopy (ARPES) confirmed the semimetallic character of $ZrTe_2$ [58], consistent with our calculations. Nonlinear optical properties of this compound have been investigated using the Z-scan method at a wavelength of 800 nm [90, 91]. $NiTe_2$, which also possesses a CdI2-type crystal structure, belongs to the SG P-3m1 (number 164). While researchers have studied the structural and electronic properties of $NiTe_2$ in nanostructures [92], the bulk and monolayer of $NiTe_2$ remain relatively unexplored. $NiTe_2$ exhibits a planar Hall effect [93] and an impressive breakdown current density value (up to $4.7 \times 10^7$ A/cm$^2$) [62]. Other studies have highlighted the potential applications of this material as an electrochemical sensor for glucose detection [94] and urea transformation [95]. Coleman et al. [96] demonstrated that layered materials like $NiTe_2$ could be efficiently exfoliated into individual layers, leading to their use in lubrication applications [97].

Over the past 40 years, numerous studies have focused on the semiconductor applications of TMDs, with $MoS_2$, $MoSe_2$, $WSe_2$, and $WTe_2$ drawing significant interest from the industry due to their

remarkable electronic and optical properties for various applications [98–101]. $WTe_2$ and $WSe_2$ are hexagonal layered crystal structures with the space group P63/mmc ($D^4_{6h}$) (No. 194) [102]. These compounds exhibit an indirect band gap, while their monolayers have a direct band gap within the range of visible to infrared light [103–105]. 2H-$WSe_2$ has been a fascinating material in photoemission studies [86, 106–108]. $WSe_2$ also shows promise as a semiconductor material for photoelectrochemical cells, solar cells, p–n junctions, and field-effect transistors [109]. Researchers have successfully fabricated field-effect transistors (FETs) from both monolayer and bulk $WSe_2$ [110]. Moreover, the study of $WSe_2$ bulk crystals primarily focuses on photovoltaic applications and photoelectrochemical hydrogen production [87, 109].

$WTe_2$, on the other hand, has unique features as a 2D material with two distinct structural phases: H and T phases [111]. The unit cells of the H and T phases are hexagonal and rectangular, respectively. Calculations have shown that the T phase is more stable than the H phase [78], thus garnering more attention. The T phase is a semimetal, while the H phase is a semiconductor, similar to several other TMDs [112–115].

This work investigates the structural, electronic, and optical properties of $ZrTe_2$, $NiTe_2$, $WTe_2$, and $WSe_2$ in both bulk and monolayer forms. We calculate structural properties, such as lattice parameters, using the GGA approach, taking into account spin–orbit coupling (SOC), and our results are consistent with previous experimental and computational findings. Furthermore, we examine electronic properties by analyzing band structures and densities of states for these compounds. We focus on optical parameters, including real and imaginary parts of the dielectric function, energy loss function, reflectivity spectra, refraction, absorption, and more. We compare the bulk and monolayer values to introduce and elaborate on the characteristics of these four compounds in two dimensions, aiming to predict their potential applications in electronic and optoelectronic devices.

## Computational methods

The density functional theory (DFT) was implemented in the WIEN2k package to investigate the structural and optical properties of $ZrTe_2$, $NiTe_2$, $WTe_2$, and $WSe_2$ bulks and monolayers [116]. The generalized gradient approximation (GGA) of Perdew–Burke Ernzerhof (PBE) formalism [117] was adopted for the exchange–correlation potential. The atomic positions of bulks and monolayers are relaxed. Meshes of 20 × 20 × 10 and 20 × 20 × 1 *k*-points in the Brillouin zone were adopted for bulks and monolayers to achieve an adequate degree of convergence. For the case of the monolayer, it was assumed that a 10 Å vacuum separates the layers to prevent interactions between periodic layers. A series of tests were performed to reach an optimal value for the cutoff parameters $R_{MT}$ $K_{\max}$=10.0 $(a.u.)^{-1}$ and magnitude of $G$ vector in reciprocal lattice $G_{\max}$=16 $(Ry)^{1/2}$. Moreover, values of the muffin-tin sphere radii ($R_{MT}$) of Zr, W, Ni, Te, and Se are 2.20, 2.18, 2.20, 2.35, and 2.37 *(a.u.)*, respectively. The same values of $R_{MT}$ $K_{\max}$ and $G_{\max}$ were used for monolayer calculations. The self-consistent calculations convergence was met when the total energy of two consecutive iterations were smaller than $10^{-5}Ry$.

## Results and discussions

### Structural properties

$ZrTe_2$ and $NiTe_2$ were crystallized in a $CdI_2$-type trigonal structure (space group *P*-3*m*1, number 164). $WTe_2$ and $WSe_2$ were crystallized in the hexagonal structure (space group $P6_3/mmc$, number 194). The crystal structures of these compounds are shown in Fig. 1, constructed by combining transition metals Zr, Ni, and W and chalcogen Te, Se. The optimized values of the lattice constants of $ZrTe_2$, $NiTe_2$, $WTe_2$, and $WSe_2$ compounds using the PBE-GGA approach were calculated and presented in Table 1, which are in good agreement with the experimental results [118–121].

Dangling bonds and free electrons were created by cutting bulk in different directions to create a monolayer. Also, the internal forces in the absence of neighboring atoms on the monolayer surface could vary from those of the unit cell in bulk and may upset the balance of the structure. Therefore, the new equilibrium condition caused the location of the atoms to increase slightly compared to the bulk state, leading to different interatomic distances, as listed in Table 2.

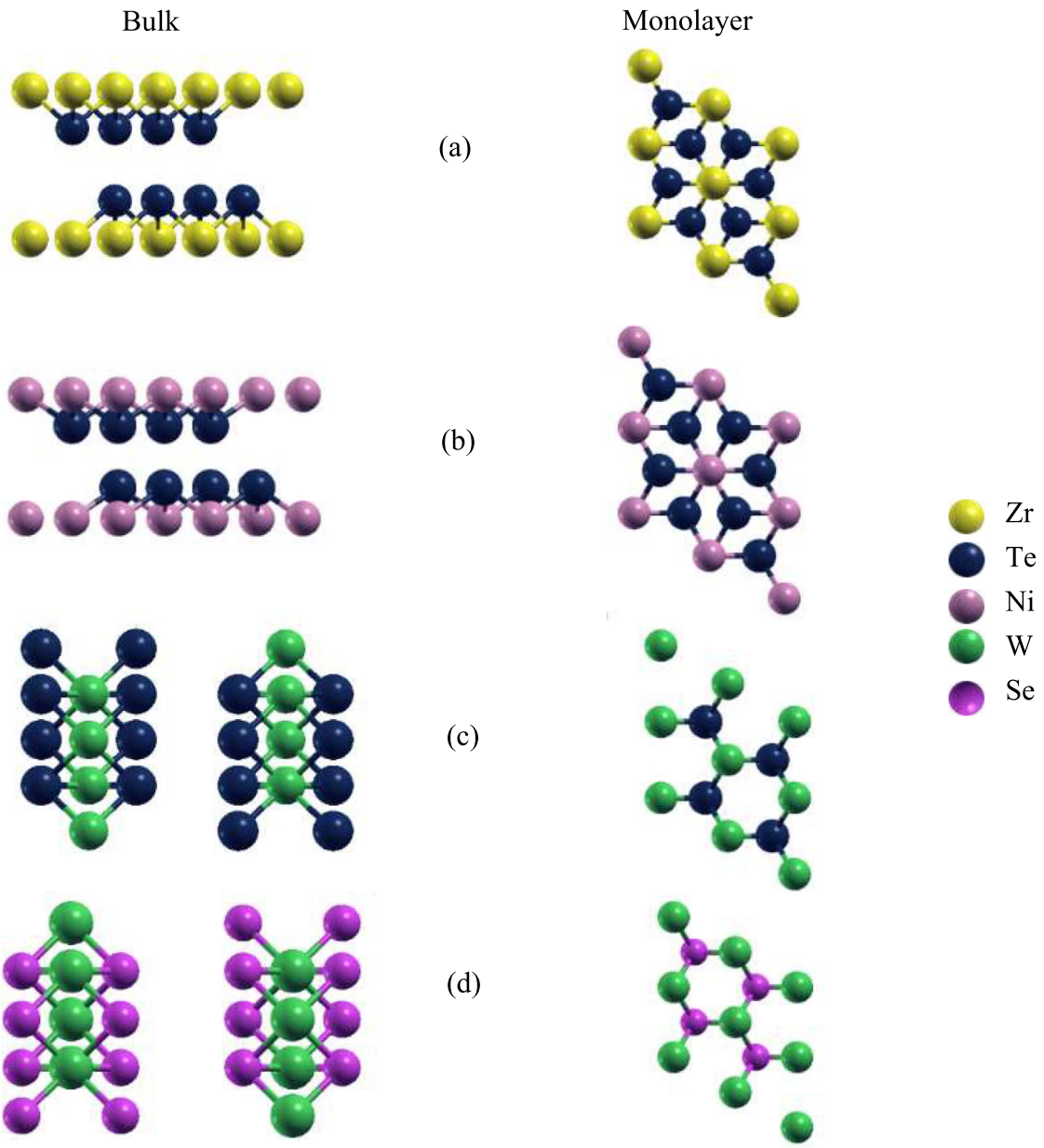


**Figure 1** The bulk and monolayer crystal structures of **a** $ZrTe_2$, **b** $NiTe_2$, **c** $WTe_2$, and **d** $WSe_2$.

## Electronic properties

The density of states and band structures were calculated for $ZrTe_2$, $NiTe_2$, $WTe_2$, and $WSe_2$ compounds to find the band gap and study the electronic properties of these compounds. According to the calculated band structure (Fig. 2) and density of states (Fig. 3), $ZrTe_2$ and $NiTe_2$ bulks have metallic behavior, while $WTe_2$ and $WSe_2$ are semimetals. The energy band gaps of these compounds are listed in Table 3 and compared with available data. The band gap of $NiTe_2$ and $ZrTe_2$ bulks is zero, which confirms the metallic behavior of these compounds. $WSe_2$ and $WTe_2$ bulks are semiconductors with estimated band gaps of 0.875 and 0.654 eV. It was found that the band gaps of monolayers are larger than their bulks, and remarkably, the $NiTe_2$ monolayer shows nonmetallic behavior. Since the GGA functionals are known to underestimate the band gaps, the $NiTe_2$ Monolayer is expected to be nonmetallic in real [122].

As can be seen in Fig. 3a the density of states of the $NiTe_2$ bulk around the Fermi energy is larger than the corresponding values of $ZrTe_2$ and has shifted

**Table 1** Optimized lattice parameters ($a=b$ in Å and c in Å) of $ZrTe_2$, $NiTe_2$, $WTe_2$, and $WSe_2$ compared to available experimental data

| Compound | a | c | c/a | Refs. |
|---|---|---|---|---|
| $ZrTe_2$ | 3.97 | 7.03 | 1.77 | This work |
| | 3.94 | 6.62 | 1.68 | [118] |
| $NiTe_2$ | 3.89 | 5.31 | 1.36 | This work |
| | 3.85 | 5.26 | 1.37 | [119] |
| $WTe_2$ | 3.56 | 14.40 | 4.04 | This work |
| | 3.60 | 14.18 | 3.93 | [120] |
| $WSe_2$ | 3.31 | 13.03 | 3.93 | This work |
| | 3.29 | 12.97 | 3.94 | [121] |

**Table 2** The interatomic distance a(Å), between transition metals (Zr, Ni, W) and chalcogen atoms (Se, Te) in $ZrTe_2$, $NiTe_2$, $WTe_2$, and $WSe_2$ bulks and monolayers

| Compound | Bulk | Monolayer |
|---|---|---|
| $ZrTe_2$ | 3.97 | 3.98 |
| $NiTe_2$ | 3.89 | 3.98 |
| $WTe_2$ | 3.56 | 3.57 |
| $WSe_2$ | 3.31 | 3.33 |

inward toward Fermi energy, indicating that the electrons in the $NiTe_2$ are more homogeneous and more substituted than the electrons in the $ZrTe_2$ [128].

Moreover, as previously mentioned and Fig. 3b indicates, since the electron density of states of both $WSe_2$ and $WTe_2$ do not cross the Fermi energy, these compounds are semiconductors with small energy gaps. The energy gap of $WTe_2$ is smaller than the energy band gap of $WSe_2$, as expected for most selenides compared to tellurides [129].

## Optical properties

The optical properties of TMDs have been of great interest for industrial applications [97]. However, the studies of monolayer TMDs are still primarily at the basic research level, pending their fundamental properties and potentially new functionalities. In this regard, the behavior of different optical quantities as a function of radiation energy must be studied to define the optical properties of these structures. Among various properties, the dielectric function, $\varepsilon(\omega)$, is the quantity with a central role in shaping the optical response [130]. All the other optical parameters, such as reflectivity, absorption coefficient, and energy loss function, can be extracted from the real and imaginary part of $\varepsilon(\omega)$, defining the intraband and interband transitions. The former is primarily used for metals [131], whereas the latter can exist for all materials containing direct and indirect transitions. At zero temperature, the indirect interband transition has a negligible contribution to $\varepsilon(\omega)$; hence it was ignored in our calculations. The imaginary part of the dielectric function disregarding the local field effects and utilizing the arbitrary phase approximation is determined by the following equation [132]:

$$\varepsilon_2(\omega) = \frac{ve^2}{2\pi\hbar\omega^2}\int \mathrm{d}^3k \sum_{mm'} \left|\left\langle \vec{k}m\middle|\vec{p}\middle|\vec{k}m'\right\rangle\right|^2 f(\vec{k}m) \times \left[1 - f(\vec{k}m')\right]\delta(E_{km} - E_{km'} - \hbar\omega), \quad (1)$$

where the integration is on all the transitions from occupied valence states to vacant conduction states. Furthermore, p and $\hbar\omega$ are the momentum operators and photon energy, respectively. The real part of the dielectric function is obtained [133] by the following relation:

$$\varepsilon_1(\omega) = 1 + \frac{2}{\pi}\int_0^\infty \frac{\varepsilon_2(\omega')\omega' d\omega'}{\omega'^2 - \omega^2}, \quad (2)$$

The dielectric function is a second-order symmetric tensor with independent elements based on crystal symmetry. Since the $ZrTe_2$, $NiTe_2$, $WTe_2$, and $WSe_2$ bulks and monolayers have hexagonal symmetry, the dielectric tensors have two independent elements. Subsequently, the optical properties of these compounds and monolayers were calculated in two electromagnetic wave polarizations, namely, parallel ($\varepsilon_{xx}(\omega)$) and perpendicular ($\varepsilon_{zz}(\omega)$) to the monolayer surface [134]. While the real part of the dielectric constant provides information regarding polarization and anomalous dispersion effects, its imaginary component explains the primary absorption energy in the crystal structure, originating from neutral charge excitations [135].

The calculated real and imaginary parts of the dielectric function of $ZrTe_2$, $NiTe_2$, $WTe_2$, and $WSe_2$ bulks within the PBE-GGA approach in both xx and zz directions are presented in Fig. 4. The real part of the static dielectric function, $\varepsilon_1(0)$, of $WTe_2$ bulk is larger than $WSe_2$ bulk. In both compounds, the Penn model [136] is fulfilled. The real part of the static dielectric function (at zero frequency) is higher than

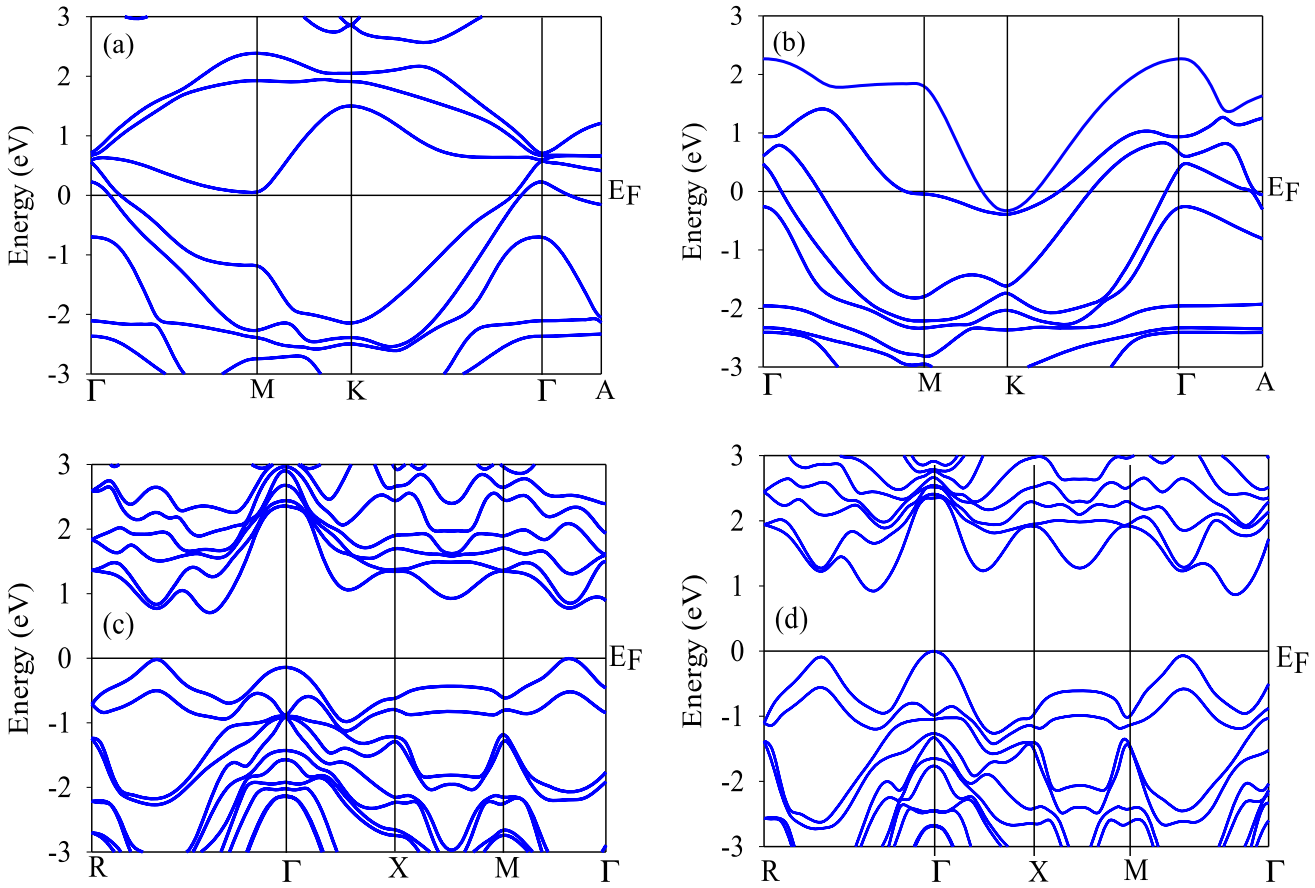


**Figure 2** The band structures of **a** $ZrTe_2$, **b** $NiTe_2$, **c** $WTe_2$, and **d** $WSe_2$ bulks. $ZrTe_2$ and $NiTe_2$ bulks are metal, whereas $WTe_2$ and $WSe_2$ are semimetals.

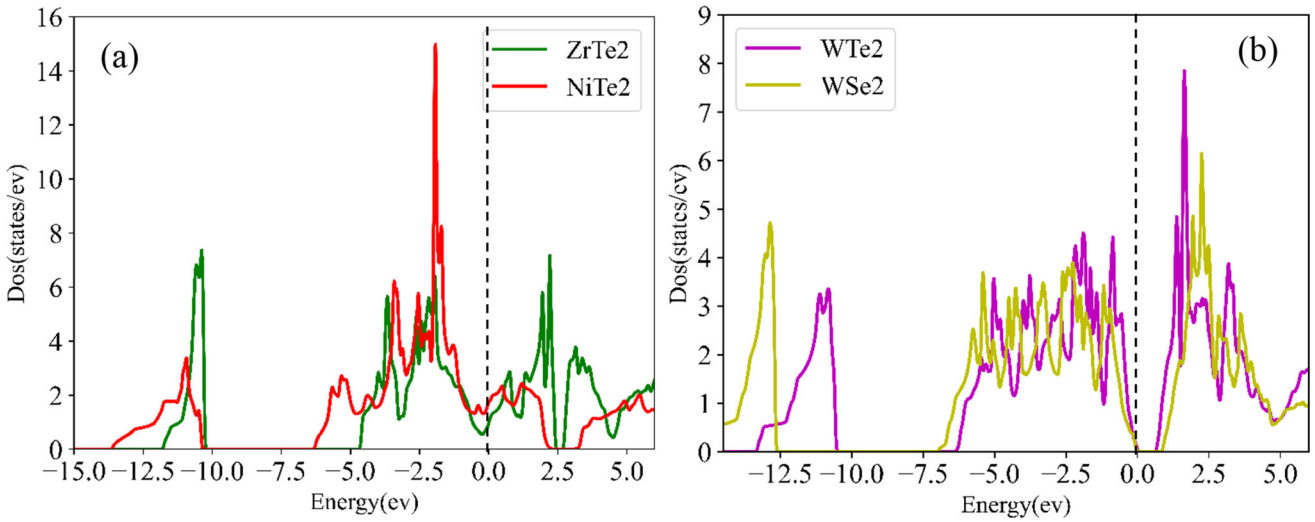


**Figure 3** The density of states of **a** $ZrTe_2$ and $NiTe_2$, **b** $WTe_2$ and $WSe_2$ bulks. $ZrTe_2$ and $NiTe_2$ compounds have metallic behavior, and $WTe_2$ and $WSe_2$ compounds are semiconductors with a small energy gap.

the imaginary part of the static dielectric function for all cases.

The peaks in the imaginary part of the dielectric function indicate interband transitions. It can be seen

**Table 3** The calculated energy band gap values of $ZrTe_2$, $NiTe_2$, $WTe_2$, and $WSe_2$ bulks and monolayers and compared to available data

| Compound | Bulk (eV) | Refs. | Monolayer (eV) | Refs. |
|---|---|---|---|---|
| $ZrTe_2$ | 0 | This work | 0 | This work |
| | 0 | [118] | 0 | [123] |
| $NiTe_2$ | 0 | This work | 0.199 | This work |
| | 0 | [124] | 0 | [125] |
| $WTe_2$ | 0.654 | This work | 0.741 | This work |
| | 0.706 | [120] | 0.974 | [126] |
| $WSe_2$ | 0.875 | This work | 1.243 | This work |
| | 1.210 | [127] | 1.420 | [121] |

that the imaginary part of the dielectric function for $ZrTe_2$ and $NiTe_2$ in the zz direction has a decreasing trend above the energy of approximately 4 eV. This value for $WSe_2$ and $WTe_2$ is larger, approximately at 6 eV. The reducing trend also happens at a higher energy for $WSe_2$ and $WTe_2$ than $ZrTe_2$ and $NiTe_2$ for the xx direction. The decreasing trend is due to the absorption of high-energy photons leading to inter-band transitions. The sudden inclination change in either the real or imaginary part of a dielectric function creates a peak in the other. The peaks observed in the imaginary part of the dielectric function indicate the maximum transition in that energy, called resonant frequencies [137]. The highest peaks of

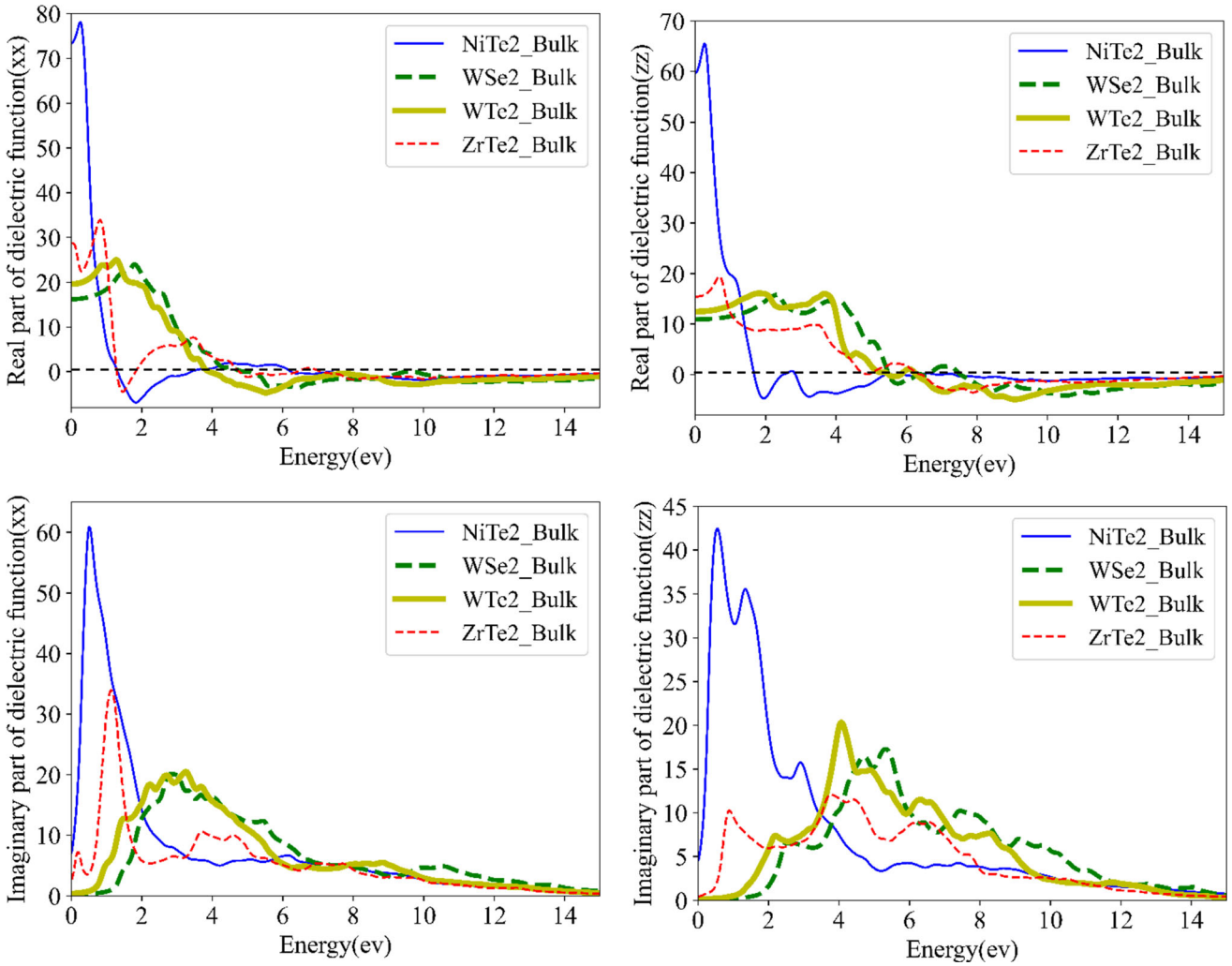


**Figure 4** Calculated plots of the real and imaginary parts of the dielectric function of $NiTe_2$, $ZrTe_2$, $WTe_2$, and $WSe_2$ within the PBE-GGA approximation in the xx (top) and zz (bottom) directions.

**Table 4** Calculated values of interband transition (IBT) peaks and $\varepsilon_1^{\parallel}(0)$ and $\varepsilon_1^{\perp}(\omega)$ of $ZrTe_2$, $NiTe_2$, $WTe_2$, and $WSe_2$ bulks

| Compound | IBT Peaks (eV) | $\varepsilon_1(0)$ |
|---|---|---|
| $NiTe_2$ | **0.50** | $\varepsilon_1^{\parallel}(0)=74$ |
| | **0.55**, 1.34, 2.89 | $\varepsilon_1^{\perp}(0)=60$ |
| $WSe_2$ | **2.81**, 3.68, 4.04, 5.42 | $\varepsilon_1^{\parallel}(0)=16$ |
| | 2.65, 4.69, **5.31**, 7.44 | $\varepsilon_1^{\perp}(0)=11$ |
| $WTe_2$ | 2.24, 2.70, **3.25**, 6.62 | $\varepsilon_1^{\parallel}(0)=19$ |
| | 2.19, **4.06**, 6.57, 8.25 | $\varepsilon_1^{\perp}(0)=12$ |
| $ZrTe_2$ | **1.12**, 2.89, 3.71 | $\varepsilon_1^{\parallel}(0)=28$ |
| | **0.88**, 2.21, 3.79, 4.39 | $\varepsilon_1^{\perp}(0)=15$ |

The prominent peaks are given in bold

$NiTe_2$, $WSe_2$, $WTe_2$, and $ZrTe_2$ are at 0.50, 2.81, 3.25, and 1.12 eV, respectively, for bulks in the xx electromagnetic wave direction. In the zz direction, the highest peaks are at 0.55, 5.31, 4.06, and 0.88 eV, respectively, as shown in Fig. 4. At the resonant frequencies, abnormal scattering occurs, which is why the real part of a dielectric function decreases with increasing energy at the resonant frequency.

According to Table 4, the calculated values of the real part of the static dielectric function ($\varepsilon_1^{\parallel}(0)$, $\varepsilon_1^{\perp}(0)$) for $NiTe_2$, $WSe_2$, $WTe_2$, and $ZrTe_2$ bulks are (74, 60), (16, 11), (19, 12), and (28, 15), respectively. $WSe_2$ has the smallest value of $\varepsilon_1(0)$, which agrees with its relatively larger band gap than the others.

The calculated real and imaginary parts of the dielectric function of both bulks and monolayers of $ZrTe_2$, $NiTe_2$, $WTe_2$, and $WSe_2$ compounds within the PBE-GGA approach are illustrated in Fig. 5. The real parts of the static dielectric function of $ZrTe_2$, $NiTe_2$, $WTe_2$, and $WSe_2$ monolayers are smaller than the corresponding values of bulks. This trend continues from zero up to 4–5 eV energies. Also, the imaginary parts of the dielectric function of the monolayers in both directions are generally smaller than the bulk values due to the larger energy gap of the monolayers. The imaginary parts of the bulk and monolayer dielectric functions at high energies approach zero, indicating that these compounds are transparent at high energies. In some energy ranges, the real part of the dielectric function is for both directions. Correspondingly, the imaginary part is low at the same energy ranges, which indicates that $ZrTe_2$, $NiTe_2$, $WTe_2$, and $WSe_2$ compounds are promising for many plasmonic applications, such as optical devices, biosensors, and photovoltaic devices [138]. This energy range (2–4 eV) is more expansive in $WTe_2$ and $WSe_2$ than in the others. Also, it is wider in the bulks of the compounds than in their monolayers.

The imaginary parts of $NiTe_2$ bulk and monolayer dielectric functions in xx direction are maximum at 0.5 eV (2481 nm). Then, they have a decreasing trend up to $\sim$ 10 eV. For the zz direction, the imaginary part for $NiTe_2$ bulk decreases above 2.9 eV (427 nm). For the monolayer, the imaginary part is significantly smaller, increasing slightly in the energy range of 0–6 eV, and dropping at higher energies.

The imaginary parts of the dielectric functions for $WSe_2$ bulk and monolayer for xx direction have increasing trends in the energy range of 0–2.9 eV and 0–2.6 eV, respectively, and decrease at higher energies. Also, in the case of zz direction, a similar trend is observed in the energy range of 0–4.6 eV for the bulk and 0–5.4 eV for the monolayer. The imaginary parts of the dielectric function of $WTe_2$ bulk and monolayer for xx direction increase up to $\sim$ 3.2 eV and decrease at higher energies. Whereas in zz direction, the peak happens at $\sim$ 4 and $\sim$ 4.3 eV for the bulk and monolayer, respectively.

Moreover, from the real part of the dielectric function, the response of $WSe_2$ and $WTe_2$ to incident light shows a high degree of anisotropic in the infrared (IR) region up to the onset of ultraviolet radiation ($E$<10 eV) and is isotropic at higher energies. In addition, the negative sign of the real part of the dielectric function ($\varepsilon_1(\omega)$) is observed in different upper UV regions for all cases, indicating no light transmission. Entirely anisotropic behaviors occur at the edge of the IR, visible, and UV regions for the light angle shown in the $\varepsilon_1(\omega)$ diagram. $\varepsilon_1(\omega)$ changes sign multiple times for $WSe_2$ and $WTe_2$ monolayers in the energy range of 4 to 15 eV, so in this energy range, significant alterations were expected in the optical response.

For $ZrTe_2$ bulk in xx and zz directions, the peaks of the imaginary parts of the dielectric functions happen at $\sim$ 3.8 and 4.4 eV, respectively. However, for the monolayer in xx and zz directions, the peaks happen at $\sim$ 1 eV (1240 nm) and $\sim$ 7.4 eV, respectively, indicating interband transitions at these energy ranges. As it can be seen in the graphs (Fig. 5), the largest response to incident light for all compounds occurs in parallel radiation, suggesting that these compounds may be suitable for the optical industry or solar cell applications [139].

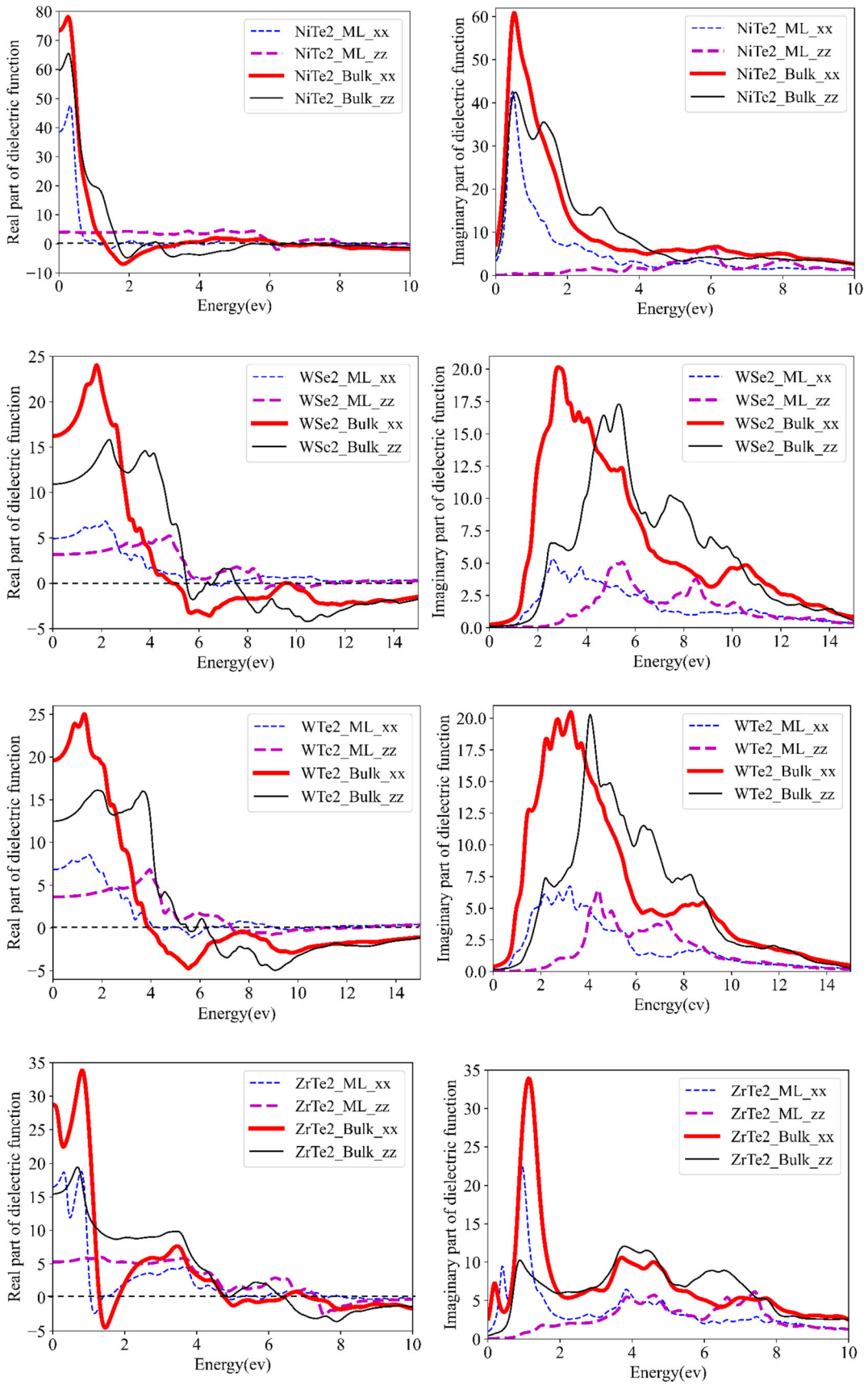
Real part of dielectric function
Energy(ev)
NiTe2_ML_xx
NiTe2_ML_zz
NiTe2_Bulk_xx
NiTe2_Bulk_zz
Imaginary part of dielectric function
Energy(ev)
NiTe2_ML_xx
NiTe2_ML_zz
NiTe2_Bulk_xx
NiTe2_Bulk_zz
Real part of dielectric function
Energy(ev)
WSe2_ML_xx
WSe2_ML_zz
WSe2_Bulk_xx
WSc2_Bulk_zz
Imaginary part of dielectric function
Energy(ev)
WSe2_ML_xx
WSe2_ML_zz
WSe2_Bulk_xx
WSe2_Bulk_zz
Real part of dielectric function
Energy(ev)
WTe2_ML_xx
WTc2_ML_zz
WTe2_Bulk_xx
WTe2_Bulk_zz
Imaginary part of dielectric function
Energy(cv)
WTe2_ML_xx
WTe2_ML_zz
WTe2_Bulk_xx
WTe2_Bulk_zz
Real part of dielectric function
Energy(ev)
ZrTe2_ML_xx
ZrTe2_ML_zz
ZrTe2_Bulk_xx
ZrTe2_Bulk_zz
Imaginary part of dielectric function
Energy(ev)
ZrTe2_ML_xx
ZrTe2_ML_zz
ZrTe2_Bulk_xx
ZrTe2_Bulk_zz

◀**Figure 5** Calculated plots of the dielectric function of $NiTe_2$, $WSe_2$, $WTe_2$, and $ZrTe_2$ bulks and monolayers within PBE-GGA approximation in xx and zz directions. The real parts of the static dielectric function of $ZrTe_2$, $NiTe_2$, $WTe_2$, and $WSe_2$ monolayers are smaller than the comparative values of their bulks.

Optical constants such as energy loss function $L(\omega)$, reflectivity $R(\omega)$, and absorption coefficient $a(\omega)$, can be calculated using the real and imaginary parts of the dielectric function by the following relations [140]:

$$L(\omega) = \frac{\varepsilon_2(\omega)}{\varepsilon_1^2(\omega) + \varepsilon_2^2(\omega)}, \tag{3}$$

$$R(\omega) = \left| \frac{\sqrt{\varepsilon_1(\omega) + i\varepsilon_2(\omega)} - 1}{\sqrt{\varepsilon_1(\omega) + i\varepsilon_2(\omega)} + 1} \right|^2, \tag{4}$$

$$a(\omega) = \frac{\sqrt{2}\omega}{c} \left( \sqrt{\varepsilon_1^2(\omega) + \varepsilon_2^2(\omega)} - \varepsilon_1(\omega) \right)^{\frac{1}{2}}. \tag{5}$$

The most substantial peaks of the energy loss in both directions for $WSe_2$ and $WTe_2$ bulks are in the energy range of 20.5–21 eV and 19–19.5 eV, respectively (Fig. 6a), which is due to plasma resonances associated with mass oscillations of the valance band electrons [141]. In comparison, the energy loss functions of $NiTe_2$ and $ZrTe_2$ are significantly lower.

Comparing the reflectivity spectra shown in Fig. 6b, it can be seen that $NiTe_2$ and $ZrTe_2$ bulk in xx direction have the highest reflectivity in the energy range of 0–5 eV. In the zz direction, $NiTe_2$ bulk behaves the same, while $ZrTe_2$ bulk has the highest value in the range of 5–10 eV. The reflectivity of $WSe_2$ and $WTe_2$ bulks in both directions are maximized in the energy ranges of 17–21 eV and 16–20 eV, respectively, and decrease monotonically at higher energies. The high reflectivities indicate that the valance electrons behave like free electrons in these energy ranges. It is also seen that $WTe_2$ and $WSe_2$ have similar shaped spectra of loss, reflectivity, and absorption in both directions, with shifts toward lower energies when Te is replaced Se in the structure. The absorption of $NiTe_2$ and $ZrTe_2$ starts at zero energy as they are both metals. The highest absorption occurs at 6–15 eV for both directions.

The calculated energy loss function, reflectivity, absorption, and refraction of $WSe_2$ and $WTe_2$ bulks and monolayers as a function of energy are shown in Fig. 7. As it can be seen in Fig. 7a, the most important peaks of the energy loss function in the xx direction of the two $WSe_2$ and $WTe_2$ monolayers are in the energy ranges of 13.1–14.7 eV and 12.8–13.1 eV, respectively. Also, in the zz direction, the most significant peaks of the two $WSe_2$ and $WTe_2$ monolayers are in the energy range of 13.9–14.4 eV, and for the $WTe_2$ monolayer, are between 12.2 and 13.7 eV. The peaks are located at lower energies in both monolayers than their bulks. The energy loss function decreases in the monolayers compared to their bulks due to the broken bonds. The coefficient values of static reflection in both monolayers and in both directions are smaller than their bulks.

According to Fig. 7b, for the $WSe_2$ compound, $R_{xx}$ for bulk is 0.91, the monolayer is 0.25, and $R_{zz}$ is 0.92 and 0.22, respectively. Also, $R_{xx}$ for $WTe_2$ bulk is 0.84, and for monolayer is 0.35, and $R_{zz}$ for bulk and monolayer are 0.86 and 0.32, respectively. The maximum reflection coefficients of the bulks in both compounds and directions occur at 16–21 eV. The corresponding values of the monolayers occur in the energy range of 5–11 eV. The maximum absorption coefficients of $WSe_2$ and $WTe_2$ monolayers in both directions are in the energy range of 6–12 eV and 5–11 eV, respectively (see Fig. 7c). Also, the absorption coefficient values of these monolayers are significantly smaller than their bulks. The monolayers and bulks are transparent in the energy range where the absorption and reflectance coefficients are small and close to zero, i.e., at energies above 20 eV for $WSe_2$ and $WTe_2$ monolayers.

As shown in Fig. 7d, the refractive index of $WSe_2$ and $WTe_2$ bulks and monolayers have their largest values at energies under 6 eV (206 nm) in both directions. Also, the refractive indexes of bulks are considerably larger than the monolayers, which can be associated with the broken bonds in the monolayer [142]. Therefore, the bulks have very high transparency and low absorption in this energy range.

The investigated energy loss function, reflectivity, absorption, and refraction of $ZrTe_2$ and $NiTe_2$ bulks and monolayers as a function of energy are illustrated in Fig. 8. The energy loss function provides a complete description of the material response to an external electromagnetic perturbation [143]. The electronic excitation is encoded in the energy loss function such that the peaks represent different features. The first fundamental peak of the energy loss function indicates the plasma resonance of electron

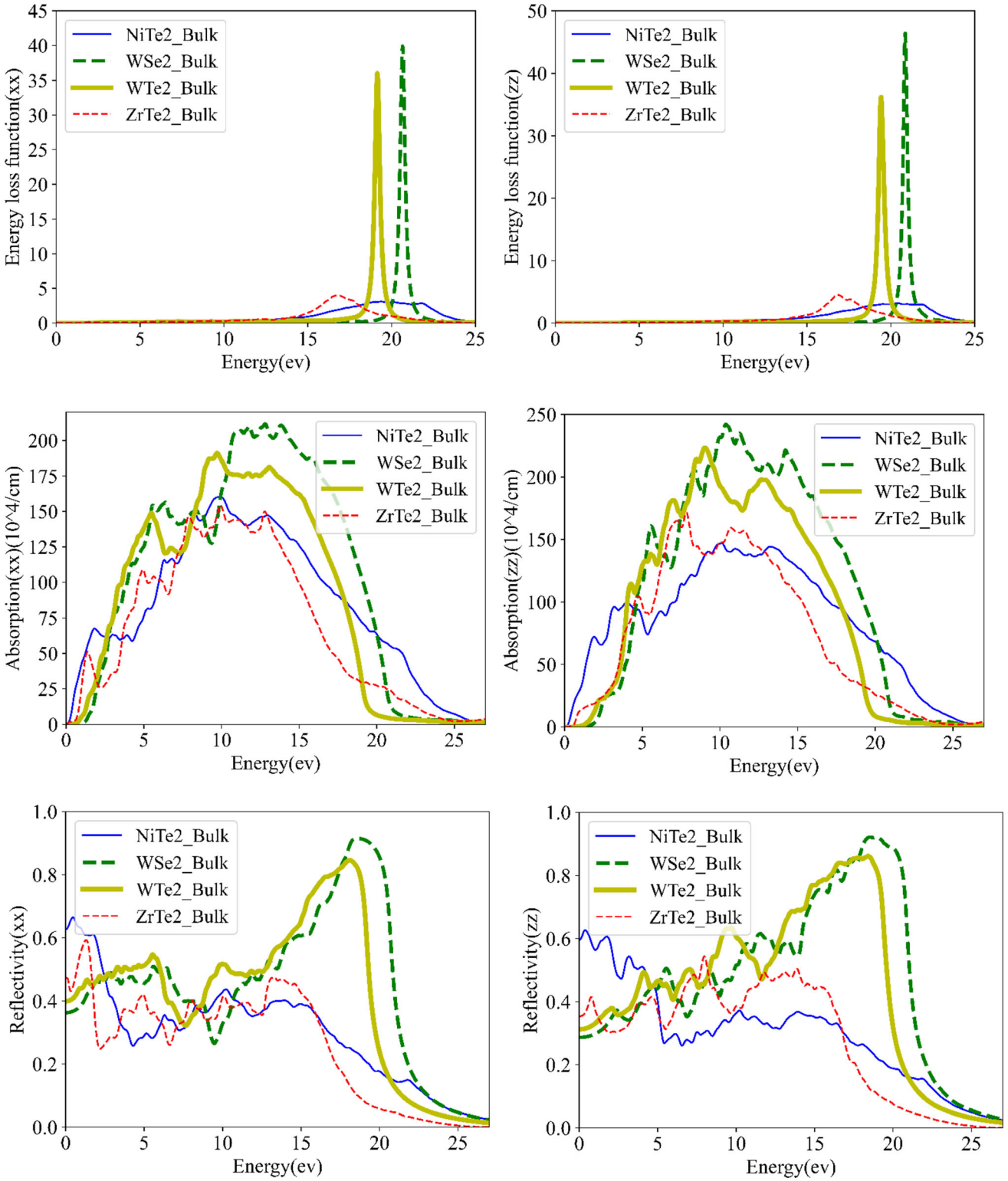


**Figure 6** The energy loss, reflectivity, and absorption of $ZrTe_2$, $NiTe_2$, $WTe_2$, and $WSe_2$ bulks in xx and zz directions. $WSe_2$ and $WTe_2$ have prominent peaks in energy loss at high energies, while the energy dissipation performance of $NiTe_2$ and $ZrTe_2$ is weak. The peaks of the reflection spectrum indicate the highest reflection, and the valleys indicate the highest absorption. The reflectivity of $WTe_2$ and $WSe_2$ is stronger for both xx and zz directions above ~ 10 eV. All materials become transparent when the reflectivity and absorption approach zero at high energies.

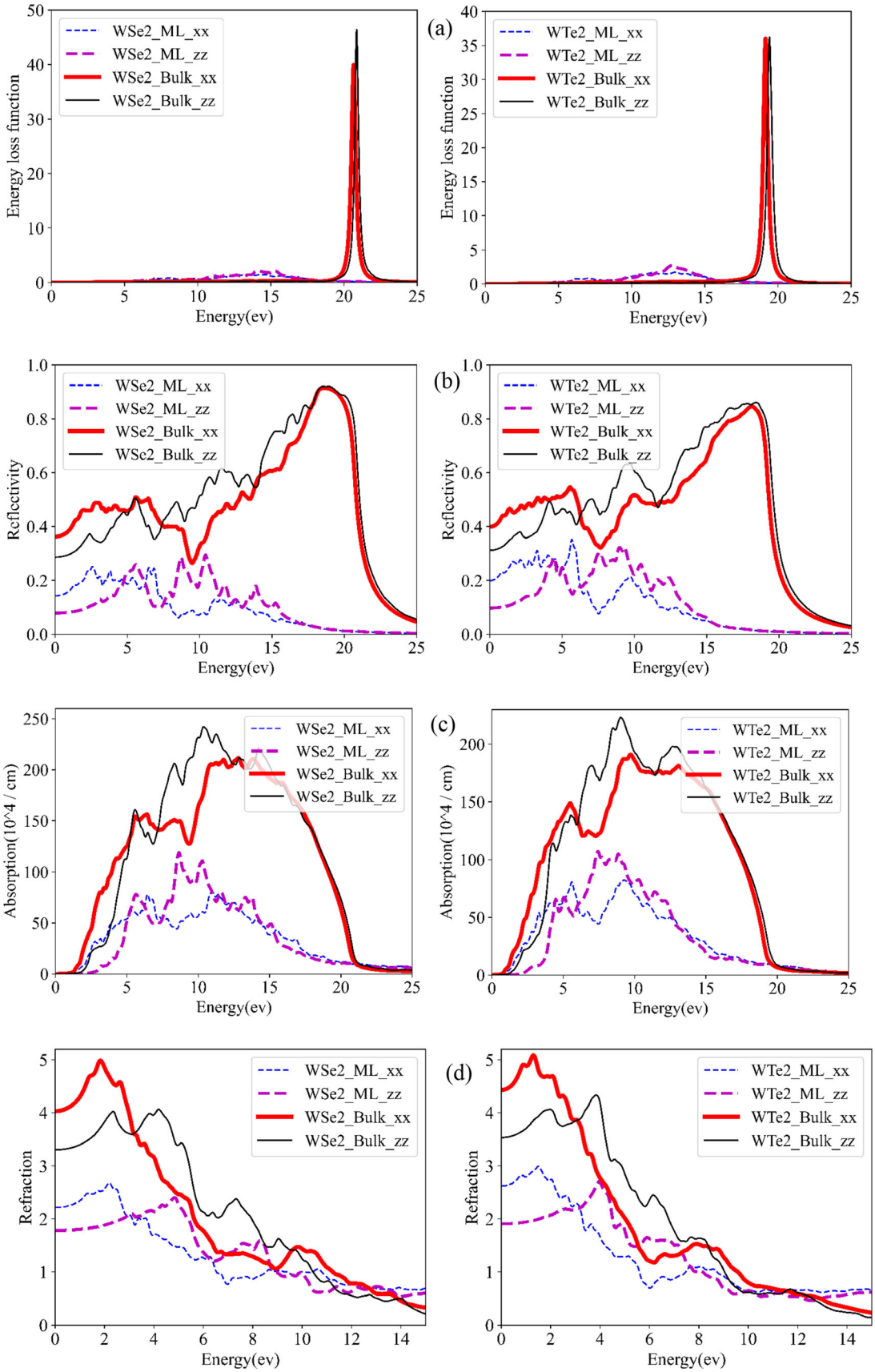
(a)
WSe2_ML_xx
WSe2_ML_zz
WSe2_Bulk_xx
WSe2_Bulk_zz
WTe2_ML_xx
WTe2_ML_zz
WTe2_Bulk_xx
WTe2_Bulk_zz
Energy loss function
Energy(ev)
(b)
Reflectivity
(c)
Absorption(10^4 / cm)
(d)
Refraction

◀**Figure 7** **a** Energy loss function, **b** reflectivity, **c** absorption, and **d** refraction of $WSe_2$ and $WTe_2$ bulks and monolayers in xx and zz directions. The energy loss peaks for both monolayers are significantly smaller than the bulk and occur at lower energies (**a**). The static reflection coefficients in both directions are smaller for the monolayers than the bulks (**b**). The absorption coefficients of these monolayers are significantly smaller than their bulks. Monolayers and bulks become transparent at high energies (> 20 eV) when the absorption and reflection coefficients approach zero (**c**). All plots show considerably smaller values for the monolayers than the bulks unless at high energies.

collective oscillations within the valence band. The other peaks are related to the interband transitions and extinctions. As clearly observed in Fig. 8a, the highest value of plasma resonance for $ZrTe_2$ Monolayer is in the energy range of 12.6–14.6 eV for both polarizations. While for $NiTe_2$ Monolayer in xx and zz directions, the maximum value occurs at an energy value within the range of 12.4–15.4 eV. The most noteworthy value of plasma resonance for $ZrTe_2$ and $NiTe_2$ compounds belongs to the x and z directions, respectively. In addition, the bulks have a higher energy loss function in both polarizations than monolayers. Subsequently, the highest plasma resonance in both polarizations occurs for bulks. The energy of the incident electromagnetic waves affects the reflectivity spectrum.

As indicated in Fig. 8b, the static reflection coefficient values in both monolayers, corresponding to xx and zz polarizations, are lower than their values of bulks. Still, the $ZrTe_2$ monolayer has two prominent peaks, the first peak, which is the highest, occurs at 1.0 eV in xx direction, and the next one at 7.8 eV in zz direction. Also, $ZrTe_2$ and $NiTe_2$ monolayers show little reflection in the energy range of 20–25 eV for both polarizations. Generally, the peaks indicate the maximum reflectivity, and valleys show the highest absorption [144]. The absorption spectrum of $ZrTe_2$ and $NiTe_2$ bulks and monolayers are plotted in Fig. 8c. The absorption spectrum can show the intraband transition from the valence to conduction bands. As expected, the absorption of $NiTe_2$ bulk is entirely different from its monolayer. The bulk of this compound has metallic behavior, while the monolayer is nonmetallic, with absorption starting from the band gap energy. The maximum absorption of $NiTe_2$ in xx direction occurs at 9.15 eV, while in the zz direction is around 8.17 eV. The highest absorption value for $ZrTe_2$ in xx and zz directions are located at 8.72 eV and 7.49 eV, respectively.

The refractive indexes of the bulks and monolayers are shown in Fig. 8d. The maximum optical transition happens in the energy ranges where the refractive index has an upward trend. It can be seen that all refractive indexes decrease with energy except for the $NiTe_2$ monolayer, which is approximately constant over the entire range of energy.

The static refractive index of $ZrTe_2$, $NiTe_2$, $WTe_2$, and $WSe_2$ bulks and monolayers are listed in Table 5. The static refractive index of bulk and Monolayer of $NiTe_2$ in xx direction have the largest values, while those of $WSe_2$ bulk and monolayer in zz direction are the smallest.

## Conclusion

In conclusion, this study presents a comprehensive analysis of the structural, electronic, and optical properties of four transition-metal dichalcogenides (TMDCs): $WTe_2$, $WSe_2$, $ZrTe_2$, and $NiTe_2$, using density functional theory (DFT) calculations. Our results show that $WSe_2$ and $WTe_2$ exhibit semiconducting behavior in both bulk and monolayer forms, while $ZrTe_2$ and $NiTe_2$ display metallic behavior in their bulk forms. However, the monolayer form of $NiTe_2$ deviates from this metallic behavior. Furthermore, we analyzed the optical characteristics, including dielectric function, reflectivity, absorption coefficient, refraction coefficient, and electron energy loss function, for both bulk and monolayer forms.

These findings offer valuable insights into the properties of these TMDCs, which can be utilized to design innovative optoelectronic devices. Notably, the monolayers of these TMDCs could be used to create transparent conductors, thanks to the decreased absorption coefficient. This work thoroughly examines the characteristics of TMDCs and their potential in various optoelectronic applications. In summary, this research highlights the importance of understanding the properties of TMDCs for the design and development of advanced optoelectronic devices.

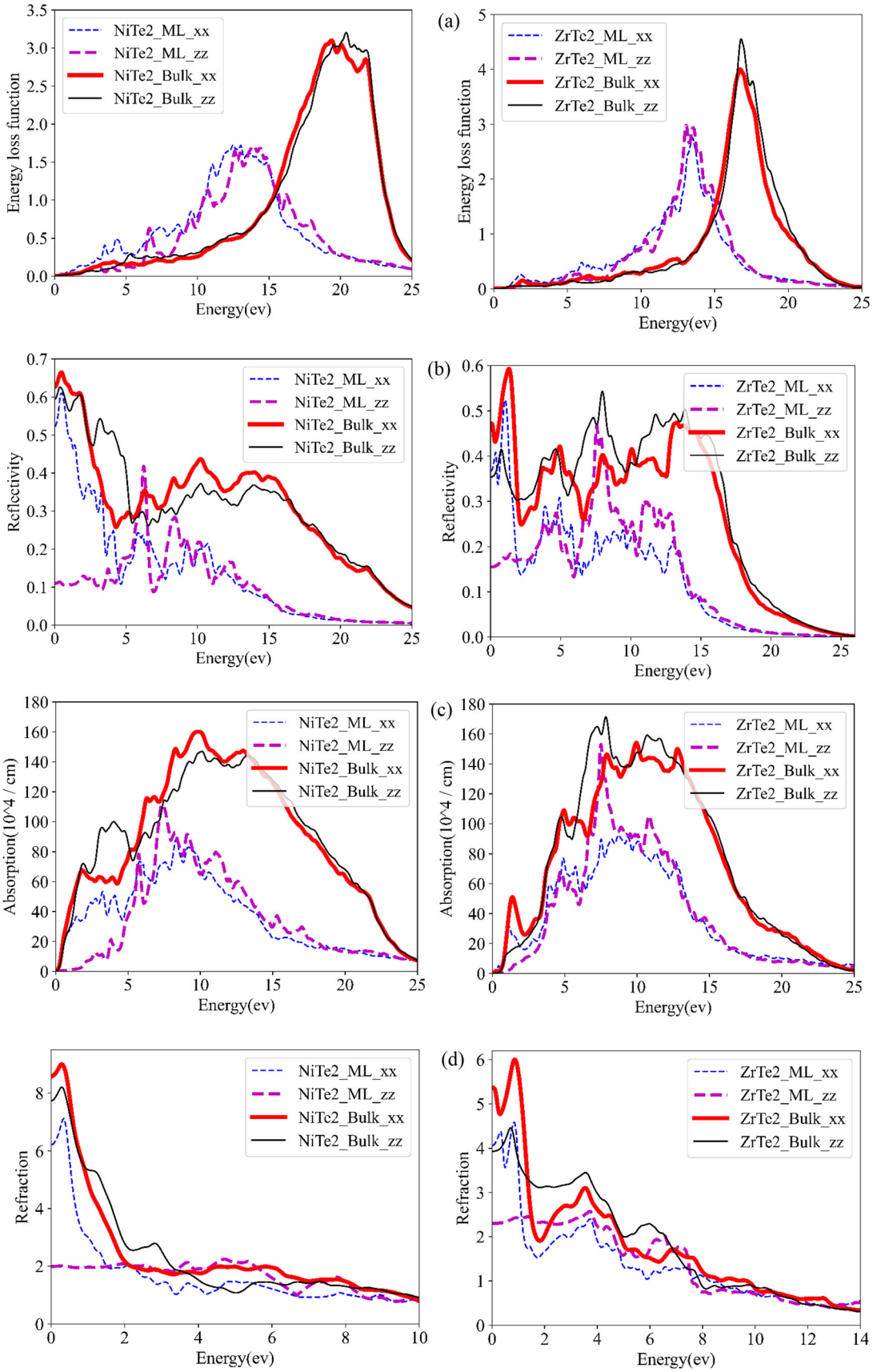
NiTe2_ML_xx
NiTe2_ML_zz
NiTe2_Bulk_xx
NiTe2_Bulk_zz
ZrTe2_ML_xx
ZrTe2_ML_zz
ZrTe2_Bulk_xx
ZrTe2_Bulk_zz
Energy loss function
Reflectivity
Absorption(10^4 / cm)
Refraction
Energy(ev)
(a)
(b)
(c)
(d)

◀**Figure 8** **a** Energy loss function, **b** reflectivity, **c** absorption coefficient, and **d** refraction coefficient of $NiTe_2$ and $ZrTe_2$ bulks and monolayers in xx and zz directions. **a** The peaks in xx and zz directions are almost the same for both materials. The static reflectivities are in the range of 0.4–0.6 for bulks and significantly smaller for the monolayers except for the $ZeTe_2$ Monolayer in xx direction, which is ~ 0.38 **b**. The absorption coefficient of $NiTe_2$ bulk is very different from that of the monolayer at low energies. The bulk shows a metallic behavior, but the monolayer shows a nonmetallic trend, with zero absorption up to the bandgap energy (**c**). The refractive indexes for all cases have a reducing trend with energy, except for the $NiTe_2$ Monolayer, which is almost constant over the entire range of energy (**d**). All plots show considerably smaller values for the monolayers than the bulks unless at high energies..

**Table 5** The static refractive index (n(ω=0)) of $ZrTe_2$, $NiTe_2$, $WTe_2$, and $WSe_2$ bulks and monolayers in both directions

| Compounds | $n_{xx}(\omega = 0)$ | $n_{zz}(\omega = 0)$ |
|---|---|---|
| $NiTe_2$ (Bulk) | 0.85 | 0.77 |
| $NiTe_2$ (ML) | 0.62 | 0.19 |
| $WSe_2$ (Bulk) | 0.40 | 0.33 |
| $WSe_2$ (ML) | 0.22 | 0.17 |
| $WTe_2$ (Bulk) | 0.44 | 0.35 |
| $WTe_2$ (ML) | 0.26 | 0.19 |
| $ZrTe_2$ (Bulk) | 0.53 | 0.39 |
| $ZrTe_2$ (ML) | 0.40 | 0.22 |

## Acknowledgements

DV acknowledges funding support from the National Science Foundation (NSF) under Grant Number CBET-2110603.

## Author's contribution

YF contributed to investigation, methodology, software, data curation, formal analysis, writing—original draft preparation, ZE contributed to data curation, software, formal analysis, validation, writing—reviewing and editing. ZN contributed to supervision, conceptualization, validation, formal analysis, resources, writing—reviewing and editing. DV contributed to supervision, validation, formal analysis, funding acquisition, writing—reviewing and editing.

## Data and code availability

The authors declare that the data used in this study are available upon request from the corresponding author within a reasonable time frame.

### Declarations

**Conflict of interest** The authors declare that they have no conflicts of interest.

**Ethical approval** Not Applicable.

## References

[1] Dahiya Y et al (2022) Modified transition metal chalcogenides for high performance supercapacitors: current trends and emerging opportunities. Coord Chem Rev 451:214265

[2] Wang X et al (2018) Few-layered WSe2 in-situ grown on graphene nanosheets as efficient anode for lithium-ion batteries. Electrochim Acta 283:1660–1667

[3] Zhou X et al (2016) Performance of a vanadium redox flow battery with a VANADion membrane. Appl Energy 180:353–359

[4] Cunha Á et al (2015) Vanadium redox flow batteries: a technology review. Int J Energy Res 39(7):889–918

[5] Yin W et al (2020) Synthesis of tungsten disulfide and molybdenum disulfide quantum dots and their applications. Chem Mater 32(11):4409–4424

[6] Tai Z et al (2022) Defected tungsten disulfide decorated CdS nanorods with covalent heterointerfaces for boosted photocatalytic H2 generation. J Colloid Interface Sci 628:252–260

[7] Wang Q et al (2016) Two-dimensional molybdenum disulfide and tungsten disulfide interleaved nanowalls constructed on silk cocoon-derived N-doped carbon fibers for hydrogen evolution reaction. Int J Hydrogen Energy 41 (47):21870–21882

[8] Dehkordi AM, Vashaee D (2012) Enhancement in thermoelectric power factor of polycrystalline Bi0. 5Sb1. 5Te3 by crystallite alignment. Phys Status Solidi (a) 209 (11):2131–2134

[9] Dresselhaus M et al (2007) Nanocomposites to enhance ZT in thermoelectrics. MRS Online Proceedings Library (OPL) 1044:1044-UO2-04

[10] Nozariasbmarz A et al (2021) Efficient self-powered wearable electronic systems enabled by microwave processed thermoelectric materials. Appl Energy 283:116211

[11] Nozariasbmarz A, Krasinski JS, Vashaee D (2019) N-type bismuth telluride nanocomposite materials optimization for thermoelectric generators in wearable applications. Materials 12(9):1529

[12] Polash MMH et al (2020) Magnon-drag thermopower in antiferromagnets versus ferromagnets. J Mater Chem C 8 (12):4049–4057

[13] Polash MMH et al (2021) Understanding and design of spin-driven thermoelectrics. Cell Rep Phys Sci 2 (11):100614

[14] Polash MMH, Rasoulianboroujeni M, Vashaee D (2020) Magnon and spin transition contribution in heat capacity of ferromagnetic Cr-doped MnTe: Experimental evidence for a paramagnetic spin-caloritronic effect. Appl Phys Lett 117 (4):043903

[15] Polash MMH, Vashaee D (2020) Magnon-bipolar carrier drag thermopower in antiferromagnetic/ferromagnetic semiconductors: Theoretical formulation and experimental evidence. Phys Rev B 102(4):045202

[16] Polash MMH, Vashaee D (2021) Anomalous thermoelectric transport properties of Fe□rich magnetic FeTe. Phys Status Solidi (RRL) Rapid Res Lett 15(10):2100231

[17] Polash MMH, Vashaee D (2021) Spin fluctuations yield zT enhancement in ferromagnets. Iscience 24(11):103356

[18] Zheng Y et al. (2019) Paramagnon drag in high thermoelectric figure of merit Li-doped MnTe. Sci Adv 5(9): eaat9461

[19] Baraeinejad B et al (2022) Design and implementation of an ultralow-power ECG patch and smart cloud-based platform. IEEE Trans Instrum Meas 71:1–11

[20] Tayebi L, Zamanipour Z, Vashaee D (2014) Design optimization of micro-fabricated thermoelectric devices for solar power generation. Renew Energy 69:166–173

[21] Polash MMH et al (2021) Topological quantum matter to topological phase conversion: fundamentals, materials, physical systems for phase conversions, and device applications. Mater Sci Eng R Rep 145:100620

[22] Lacroix M et al. (1989) Hydrogenating properties of unsupported transition metal sulfides. J Catalysis, USA, 120(2)

[23] Delgado AD et al (2022) Monolayer CoMoS catalysts on hierarchically porous alumina spheres as bifunctional nanomaterials for hydrodesulfurization and energy storage applications. Catalysts 12(8):913

[24] Lee HJ et al (2019) Ultrahigh-mobility and solution-processed inorganic P-channel thin-film transistors based on a transition-metal halide semiconductor. ACS Appl Mater Interfaces 11(43):40243–40251

[25] Pang C et al (2021) High-performance inorganically connected CuInSe2 nanocrystal thin-film transistors and integrated circuits based on the solution process of colloidal synthesis, ligand exchange, and surface treatment. Chem Mater 33(22):8775–8785

[26] Khan MAU et al (2020) Analytical current transport modeling of monolayer molybdenum disulfide-based dual gate tunnel field effect transistor. IEEE Trans Nanotechnol 19:620–627

[27] Lator E (2019) Superconductivity In Layered Transition Metal (Di) chalcogenides: Iron Selenide And Niobium Diselenide. UCL (University College London)

[28] Cheng F et al (2018) Epitaxial growth of single-layer niobium selenides with controlled stoichiometric phases. Adv Mater Interfaces 5(15):1800429

[29] Grahlow F et al (2021) Formation of a polar structure in the metallic niobium sulfide Nb4S3. Inorg Chem 60 (23):17669–17676

[30] Bucher E (1992) Photovoltaic properties of solid state junctions of layered semiconductors. Photoelectrochem Photovoltaics Layered Semiconductors, pp 1–81

[31] Ramasami AK, Reddy M, Balakrishna GR (2015) Combustion synthesis and characterization of NiO nanoparticles. Mater Sci Semicond Process 40:194–202

[32] Li J et al. (2020) Structural and elastic properties of WSe2: first-principles calculations. J Phys Conf Ser. IOP Publishing

[33] Wilson JA, Yoffe A (1969) The transition metal dichalcogenides discussion and interpretation of the observed optical, electrical and structural properties. Adv Phys 18 (73):193–335

[34] Yoffe A (1973) Layer compounds. Annu Rev Mater Sci 3 (1):147–170

[35] Yoffe AD (1993) Low-dimensional systems: quantum size effects and electronic properties of semiconductor microcrystallites (zero-dimensional systems) and some quasi-two-dimensional systems. Adv Phys 42(2):173–262

[36] Canpolat M et al (2019) Structural and electronic properties of BiOF with two-dimensional layered structure under high pressure: Ab initio study. Solid State Commun 288:33–37

[37] Radisavljevic B, Whitwick MB, Kis A (2011) Integrated circuits and logic operations based on single-layer MoS2. ACS Nano 5(12):9934–9938

[38] Hwang WS et al. (2012) First demonstration of two-dimensional WS 2 transistors exhibiting 10 5 room temperature modulation and ambipolar behavior. In: 70th Device research conference. IEEE

[39] Ilatikhameneh H et al (2015) Tunnel field-effect transistors in 2-D transition metal dichalcogenide materials. IEEE J Explor Solid State Comput Devices Circuits 1:12–18

[40] Kang J et al (2013) Band offsets and heterostructures of two-dimensional semiconductors. Appl Phys Lett 102 (1):012111
[41] Gong C et al (2013) Band alignment of two-dimensional transition metal dichalcogenides: application in tunnel field effect transistors. Appl Phys Lett 103(5):053513
[42] Li M et al (2014) Single particle transport in two-dimensional heterojunction interlayer tunneling field effect transistor. J Appl Phys 115(7):074508
[43] Yin Z et al (2012) Single-layer MoS2 phototransistors. ACS Nano 6(1):74–80
[44] Perea-López N et al (2013) Photosensor device based on few-layered WS2 films. Adv Func Mater 23(44):5511–5517
[45] Perkins FK et al (2013) Chemical vapor sensing with monolayer MoS2. Nano Lett 13(2):668–673
[46] Lu Y et al (2010) DNA-decorated graphene chemical sensors. Appl Phys Lett 97(8):083107
[47] Wang L et al (2014) Functionalized MoS2 nanosheet-based field-effect biosensor for label-free sensitive detection of cancer marker proteins in solution. Small 10(6):1101–1105
[48] Lee J et al (2013) High frequency MoS2 nanomechanical resonators. ACS Nano 7(7):6086–6091
[49] Kaul AB (2013) Nano-electro-mechanical-systems (NEMS) and energy-efficient electronics and the emergence of two-dimensional layered materials beyond graphene. In: Micro Nanotechnol Sens Syst Appl V. SPIE
[50] Yalameha S et al (2021) Promising bialkali bismuthides Cs (Na, K) 2Bi for high-performance nanoscale electromechanical devices: prediction of mechanical and anisotropic elastic properties under hydrostatic tension and compression and tunable auxetic properties. Nanomaterials 11 (10):2739
[51] Uchoa B, Cabrera G, Neto AC (2005) Nodal liquid and s-wave superconductivity in transition metal dichalcogenides. Phys Rev B 71(18):184509
[52] Yun WS et al (2012) Thickness and strain effects on electronic structures of transition metal dichalcogenides: 2H-M X 2 semiconductors (M= Mo, W; X= S, Se, Te). Phys Rev B 85(3):033305
[53] Pumera M, Sofer Z, Ambrosi A (2014) Layered transition metal dichalcogenides for electrochemical energy generation and storage. J Mater Chem A 2(24):8981–8987
[54] Chee SS et al (2020) Atomic vacancy control and elemental substitution in a monolayer molybdenum disulfide for high performance optoelectronic device arrays. Adv Func Mater 30(11):1908147
[55] Wang Z et al (2020) A noble metal dichalcogenide for high-performance field-effect transistors and broadband photodetectors. Adv Func Mater 30(5):1907945
[56] Shi S et al (2020) FeP quantum dots confined in carbon-nanotube-grafted P-doped carbon octahedra for high-rate sodium storage and full-cell applications. Adv Func Mater 30(10):1909283
[57] Cui Y et al (2020) Controlled design of well-dispersed ultrathin MoS2 nanosheets inside hollow carbon skeleton: toward fast potassium storage by constructing spacious "houses" for K ions. Adv Func Mater 30(10):1908755
[58] Tay RY et al (2020) Lightweight, superelastic boron nitride/polydimethylsiloxane foam as air dielectric substitute for multifunctional capacitive sensor applications. Adv Func Mater 30(10):1909604
[59] Shen J et al (2018) 2D MXene nanofilms with tunable gas transport channels. Adv Func Mater 28(31):1801511
[60] Bozheyev F, Ellmer K (2022) Thin film transition metal dichalcogenide photoelectrodes for solar hydrogen evolution: a review. J Mater Chem A
[61] Bernede J, Pouzet J, Alaoui Z (1990) Preparation and characterization of molybdenum diselenide thin films. Appl Phys A 51:155–159
[62] Zhao B et al (2018) Synthetic control of two-dimensional NiTe2 single crystals with highly uniform thickness distributions. J Am Chem Soc 140(43):14217–14223
[63] Radisavljevic B et al (2011) Single-layer MoS2 transistors. Nat Nanotechnol 6(3):147–150
[64] Larentis S, Fallahazad B, Tutuc E (2012) Field-effect transistors and intrinsic mobility in ultra-thin MoSe2 layers. Appl Phys Lett 101(22):223104
[65] Bernardi M, Palummo M, Grossman JC (2013) Extraordinary sunlight absorption and one nanometer thick photovoltaics using two-dimensional monolayer materials. Nano Lett 13(8):3664–3670
[66] Lagarde D et al (2014) Carrier and polarization dynamics in monolayer MoS 2. Phys Rev Lett 112(4):047401
[67] Mak KF et al (2012) Control of valley polarization in monolayer MoS2 by optical helicity. Nat Nanotechnol 7 (8):494–498
[68] Zeng H et al (2012) Valley polarization in MoS2 monolayers by optical pumping. Nat Nanotechnol 7(8):490–493
[69] Geim AK, Grigorieva IV (2013) Van der Waals heterostructures. Nature 499(7459):419–425
[70] Wu S et al (2015) Monolayer semiconductor nanocavity lasers with ultralow thresholds. Nature 520(7545):69–72
[71] Manzeli S et al (2017) 2D transition metal dichalcogenides. Nat Rev Mater 2(8):1–15
[72] Wang QH et al (2012) Electronics and optoelectronics of two-dimensional transition metal dichalcogenides. Nat Nanotechnol 7(11):699–712

[73] Chhowalla M et al (2013) The chemistry of two-dimensional layered transition metal dichalcogenide nanosheets. Nat Chem 5(4):263–275
[74] Soluyanov AA et al (2015) Type-ii weyl semimetals. Nature 527(7579):495–498
[75] ElGhazali MA et al. (2017) Pressure-induced superconductivity up to 13.1 K in the pyrite phase of palladium diselenide PdS e 2. Phys Rev B 96(6):060509
[76] Nourbakhsh A et al (2016) MoS2 field-effect transistor with sub-10 nm channel length. Nano Lett 16(12):7798–7806
[77] Fang L et al (2005) Fabrication and superconductivity of Na x Ta S 2 crystals. Phys Rev B 72(1):014534
[78] Wagner K et al (2008) Tuning the charge density wave and superconductivity in Cu x TaS 2. Phys Rev B 78 (10):104520
[79] Jishi R, Alyahyaei H (2008) Electronic structure of superconducting copper intercalated transition metal dichalcogenides: first-principles calculations. Phys Rev B 78 (14):144516
[80] Morosan E et al (2010) Multiple electronic transitions and superconductivity in Pd x TiSe 2. Phys Rev B 81 (9):094524
[81] Kiswandhi A et al (2013) Competition between the structural phase transition and superconductivity in Ir 1–x Pt x Te 2 as revealed by pressure effects. Phys Rev B 87 (12):121107
[82] Chang T-R et al (2016) Topological Dirac surface states and superconducting pairing correlations in PbTaSe 2. Phys Rev B 93(24):245130
[83] Guzman D, Onofrio N, Strachan A (2017) First principles investigation of copper and silver intercalated molybdenum disulfide. J Appl Phys 121(5):055703
[84] Kumar A, Ahluwalia P (2012) Electronic structure of transition metal dichalcogenides monolayers 1H-MX 2 (M= Mo, W; X= S, Se, Te) from ab-initio theory: new direct band gap semiconductors. Eur Phys J B 85(6):1–7
[85] Kam K, Parkinson B (1982) Detailed photocurrent spectroscopy of the semiconducting group VIB transition metal dichalcogenides. J Phys Chem 86(4):463–467
[86] Coehoorn R, Haas C, De Groot R (1987) Electronic structure of MoSe 2, MoS 2, and WSe 2. II. The nature of the optical band gaps. Phys Rev B 35(12):6203
[87] Tenne R, Wold A (1985) Passivation of recombination centers in n-WSe2 yields high efficiency (> 14%) photoelectrochemical cell. Appl Phys Lett 47(7):707–709
[88] Sienicki W, Hryniewicz T (1996) Tungsten diselenide heterojunction photoelectrodes. Sol Energy Mater Sol Cells 43(1):67–72
[89] Villaos RAB et al (2021) Evolution of the electronic properties of ZrX2 (X= S, Se, or Te) thin films under varying thickness. J Phys Chem C 125(1):1134–1142
[90] Sheik-Bahae M, Van Stryland EW (1999) Optical nonlinearities in the transparency region of bulk semiconductors. UNIVERSITY OF CENTRAL FLORIDA ORLANDO
[91] De Araújo CB, Gomes AS, Boudebs G (2016) Techniques for nonlinear optical characterization of materials: a review. Rep Prog Phys 79(3):036401
[92] Dulal RP et al (2019) Nanostructures of type-II topological Dirac semimetal NiTe2. J Vac Sci Technol B Nanotechnol Microelectron Mater Process Meas Phenom 37(4):042903
[93] Liu Q et al (2019) Nontopological origin of the planar Hall effect in the type-II Dirac semimetal NiTe 2. Phys Rev B 99 (15):155119
[94] Li Y et al (2018) Porous NiTe2 nanosheet array: An effective electrochemical sensor for glucose detection. Sens Actuators B Chem 274:427–432
[95] Wang Z et al (2019) Rational design of metallic NiTe x (x= 1 or 2) as bifunctional electrocatalysts for efficient urea conversion. ACS Appl Energy Mater 2(5):3363–3372
[96] Coleman JN et al (2011) Two-dimensional nanosheets produced by liquid exfoliation of layered materials. Science 331(6017):568–571
[97] Kumar A, Ahluwalia P (2012) Electronic structure of transition metal dichalcogenides monolayers 1H-MX 2 (M= Mo, W; X= S, Se, Te) from ab-initio theory: new direct band gap semiconductors. Eur Phys J B 85:1–7
[98] Smith RJ et al (2011) Large-scale exfoliation of inorganic layered compounds in aqueous surfactant solutions. Adv Mater 23(34):3944–3948
[99] Liu B et al (2010) Pressure induced semiconductor-semimetal transition in WSe2. J Phys Chem C 114(33):14251–14254
[100] Ansari R, Malakpour S, Faghihnasiri M (2014) Effects of in-plane electric field and temperature change on Young's modulus of hexagonal boron nitride nanosheets with different chiralities. Superlattices Microstruct 68:16–26
[101] Ahmadi A et al (2019) Strain induced NDR and rectification behavior of the γ-graphyne nanotubes. Mater Res Exp 6(4):045050
[102] Schutte W, De Boer J, Jellinek F (1987) Crystal structures of tungsten disulfide and diselenide. J Solid State Chem 70 (2):207–209
[103] Mak KF et al (2010) Atomically thin MoS 2: a new direct-gap semiconductor. Phys Rev Lett 105(13):136805
[104] Ansari R et al (2013) Structural and elastic properties of carbon nanotubes containing Fe atoms using first principles. Superlattices Microstruct 64:220–226

[105] Ahmadi A et al (2019) Nonlinear Electronic transport behavior of $\Upsilon $-graphyne nanotubes. IEEE Trans Electron Devices 66(3):1584–1590
[106] Straub T et al (1996) Valence-band maximum in the layered semiconductor W Se 2: Application of constant-energy contour mapping by photoemission. Phys Rev B 53(24): R16152
[107] Finteis T et al (1997) Occupied and unoccupied electronic band structure of WSe 2. Phys Rev B 55(16):10400
[108] Traving M et al (1997) Electronic structure of WSe 2: A combined photoemission and inverse photoemission study. Phys Rev B 55(16):10392
[109] Lewerenz H, Heller A, DiSalvo F (1980) Relationship between surface morphology and solar conversion efficiency of tungsten diselenide photoanodes. J Am Chem Soc 102(6):1877–1880
[110] Zhu C et al (2011) Structural transitions of NaAlH4 under high pressure by first-principles calculations. Phys B 406 (8):1612–1614
[111] Torun E et al (2016) Anisotropic electronic, mechanical, and optical properties of monolayer WTe2. J Appl Phys 119 (7):074307
[112] Jana MK et al (2015) A combined experimental and theoretical study of the structural, electronic and vibrational properties of bulk and few-layer Td-WTe2. J Phys Condens Matter 27(28):285401
[113] Brown BE (1966) The crystal structures of WTe2 and high-temperature MoTe2. Acta Crystallogr A 20(2):268–274
[114] Dawson W, Bullett D (1987) Electronic structure and crystallography of MoTe2 and WTe2. J Phys C Solid State Phys 20(36):6159
[115] Pizzochero M, Yazyev OV (2018) Single-layer 1T′-MoS2 under electron irradiation from ab initio molecular dynamics. 2D Mater 5(2):025022
[116] Blaha P (1991) A full potential linearized augmented plane wave package for calculating crystal properties. Karlheinz Schwarz. Techn. Universit at Wien, Austria
[117] Perdew JP, Burke K, Ernzerhof M (1996) Generalized gradient approximation made simple. Phys Rev Lett 77 (18):3865
[118] Kar I et al (2020) Metal-chalcogen bond-length induced electronic phase transition from semiconductor to topological semimetal in Zr X 2 (X= Se and Te). Phys Rev B 101(16):165122
[119] Xu C et al (2018) Topological type-II Dirac fermions approaching the Fermi level in a transition metal dichalcogenide NiTe2. Chem Mater 30(14):4823–4830
[120] Lee CH (2015) Tungsten ditelluride (WTe2): an atomic layered semimetal
[121] Delphine SM, Jayachandran M, Sanjeeviraja C (2003) Pulsed electrodeposition and characterisation of tungsten diselenide thin films. Mater Chem Phys 81(1):78–83
[122] Mao Y et al (2023) The electronic, mechanical properties and in-plane negative Poisson's ratio in novel pentagonal NiX2 (X= S, Se, Te) monolayers with strong anisotropy: a first-principles prediction. Comput Mater Sci 216:111873
[123] Guo H et al (2014) Tuning electronic and magnetic properties of early transition-metal dichalcogenides via tensile strain. J Phys Chem C 118(13):7242–7249
[124] Qi M et al (2020) Pressure-driven Lifshitz transition in type-II Dirac semimetal NiTe 2. Phys Rev B 101 (11):115124
[125] Aras M, Kılıç Ç, Ciraci S (2020) Magnetic ground state in FeTe 2, VS 2, and NiTe 2 monolayers: Antiparallel magnetic moments at chalcogen atoms. Phys Rev B 101 (5):054429
[126] Islam MR et al (2022) Impact of strain on the electronic, phonon, and optical properties of monolayer transition metal dichalcogenides XTe2 (X= Mo and W). Phys Scr 97 (4):045806
[127] Gusakova J et al. (2017) Electronic properties of bulk and monolayer TMDs: theoretical study within DFT framework (GVJ□2e method). Phys Status Solidi (a) 214(12):1700218
[128] Zhao B et al (2021) 2D metallic transition-metal dichalcogenides: structures, synthesis, properties, and applications. Adv Func Mater 31(48):2105132
[129] Luo Y et al (2021) First-principles study on band gaps and transport properties of van der Waals WSe2/WTe2 heterostructure. Zeitschrift für Naturforschung A 76 (4):361–370
[130] Li Y et al (2014) Measurement of the optical dielectric function of monolayer transition-metal dichalcogenides: MoS 2, Mo S e 2, WS 2, and WS e 2. Phys Rev B 90 (20):205422
[131] Nourbakhsh Z (2010) Structural, electronic and optical properties of ZnX and CdX compounds (X= Se, Te and S) under hydrostatic pressure. J Alloy Compd 505(2):698–711
[132] Ambrosch-Draxl C, Sofo JO (2006) Linear optical properties of solids within the full-potential linearized augmented planewave method. Comput Phys Commun 175 (1):1–14
[133] Slassi A et al (2015) Ab initio study on the electronic, optical and electrical properties of Ti-, Sn- and Zr-doped ZnO. Solid State Commun 218:45–48
[134] Narimani M, Nourbakhsh Z (2017) Topological phase and optical properties of LuNiBi bulk and nano-layer. Thin Solid Films 634:112–120
[135] Pandey N, Kumar A, Chakrabarti S (2019) Investigation of the structural, electronic, and optical properties of Mn-

doped CsPbCl 3: theory and experiment. RSC Adv 9 (51):29556–29565
[136] Penn DR (1962) Wave-number-dependent dielectric function of semiconductors. Phys Rev 128(5):2093
[137] Lamsal C, Ravindra N (2013) Optical properties of vanadium oxides-an analysis. J Mater Sci 48:6341–6351
[138] Barbillon G (2019) Plasmonics and its Applications. Multidisciplinary Digital Publishing Institute
[139] Dias A et al (2021) Excitonic effects on two-dimensional transition-metal dichalcogenide monolayers: impact on solar cell efficiency. ACS Appl Energy Mater 4(4):3265–3278
[140] Saha S, Sinha T, Mookerjee A (2000) Electronic structure, chemical bonding, and optical properties of paraelectric BaTiO 3. Phys Rev B 62(13):8828
[141] Kumar A, Ahluwalia P (2012) Tunable dielectric response of transition metals dichalcogenides MX2 (M= Mo, W; X= S, Se, Te): Effect of quantum confinement. Phys B 407 (24):4627–4634
[142] Voshell A, Terrones M, Rana M (2018) Review of optical properties of two-dimensional transition metal dichalcogenides. Wide Bandgap Power Energy Devices Appl III (10754):66–83
[143] Sun Y et al (2016) Calculations of energy-loss function for 26 materials. Chin J Chem Phys 29(6):663–670
[144] Koperski M et al (2017) Optical properties of atomically thin transition metal dichalcogenides: observations and puzzles. Nanophotonics 6(6):1289–1308